Liquid Crystals
Publication details, including instructions for authors and subscription information:
http://www.informaworld.com/smpp/title~content=t713926090

Freeze-fracture electron microscopy of lyotropic lipid systems Quantitative analysis of cubic phases of space group Ia3d (Q^{230})

H. Delacroix[a]; T. Gulik-krzywicki[a]; P. Mariani[b]; J. -L. Risler[a]
[a] Centre de Génétique Moléculaire, Laboratoire Propre du CNRS associé à l'Université Pierre et Marie Curie, Gif-sur-Yvette Cedex, France [b] Istituto di Scienze Fisiche, Università degli Studi di Ancona, Ancona, Italy

To cite this Article Delacroix, H. , Gulik-krzywicki, T. , Mariani, P. and Risler, J. -L.(1993) 'Freeze-fracture electron microscopy of lyotropic lipid systems Quantitative analysis of cubic phases of space group Ia3d (Q^{230})', Liquid Crystals, 15: 5, 605 — 625

To link to this Article: DOI: 10.1080/02678299308036481

URL: http://dx.doi.org/10.1080/02678299308036481

LIQUID CRYSTALS, 1993, VOL. 15, NO. 5, 605–625

Freeze–fracture electron microscopy of lyotropic lipid systems
Quantitative analysis of cubic phases of space group Ia3d (Q^{230})

by H. DELACROIX†*, T. GULIK-KRZYWICKI†, P. MARIANI‡
and J.-L. RISLER†

† Centre de Génétique Moléculaire, Laboratoire Propre du CNRS associé
à l'Université Pierre et Marie Curie, Avenue de la Terrasse,
F-91198 Gif-sur-Yvette Cedex, France

‡Istituto di Scienze Fisiche, Università degli Studi di Ancona,
via Ranieri, 65, I-60131 Ancona, Italy

(*Received 10 September 1992; accepted 12 May 1993*)

The cubic phases Q^{230} (space group Ia3d) of type I (oil in water) and type II (water in oil) have been studied by freeze–fracture electron microscopy. The preservation of the sample structure during cryofixation was verified by low temperature X-ray diffraction. Three types of fracture planes were clearly identified in the type I system and two in the type II system. These fracture planes showed two-dimensionally ordered domains, each subdivided into subdomains related to each other by displacements and rotations compatible with the symmetry of the space group. The images were filtered using correlation averaging techniques and the filtered images were compared with the corresponding sections of the electron density map. Several conclusions were drawn: (i) The structures of the samples had been preserved after quenching, fracturing and replicating processes. (ii) The electron microscope images were fully compatible with the postulated space group symmetries. (iii) The fracture planes coincide with the planes giving rise to the most intense X-ray reflections and containing the rod-like structure elements that seem to facilitate the propagation of the fractures. This approach constitutes a new and powerful tool of general interest for the study of liquid crystals.

1. Introduction

Electron microscopy has been used only sparingly for the study of pure lipid–water phases. The study of untreated samples is virtually impossible, firstly, because of the damaging effects of both the high vacuum and the electron beam and secondly, because of the very weak contrast intrinsic to systems consisting of lipids and water. Additionally, there is the concern that pretreatments, such as chemical fixation or staining, will alter the structure of the sample. The best way of avoiding these pitfalls is cryofixation, provided the sample is quenched fast enough, temperature-induced structural alterations, ice crystal formation, etc, can be avoided. This may not be achieved in practice and it is desirable to assess the degree of preservation of the structure during cryofixation. The combined use of low temperature X-ray scattering and freeze–fracture electron microscopy has been developed for this purpose and

---

*Author for correspondence.

applied to a variety of lipid–water and protein–lipid–water phases of known structure [1–3]. In the case of lamellar and hexagonal phases, the freeze–fracture images of properly frozen samples are in excellent agreement with the structure, as determined by X-ray scattering studies (see for example, Gulik-Krzywicki *et al.* [3]). In particular, for the more ordered lipid phases, excellent results have been obtained, which have played a useful role in the subsequent structural analysis [4, 5].

The present work is focused on phases with cubic symmetry. Since their discovery in the late 1950s, 6 cubic phases have been identified in lipid-containing systems and studied by X-ray diffraction techniques (reviewed by Mariani *et al.* [6]).

Although X-ray crystallography has been the main technique used for structural analysis of these cubic phases, other techniques, such as lateral diffusion measurements, both by NMR [7, 8] and by fluorescence recovery after photo-bleaching [9] have provided interesting complementary data. As far as electron microscopy is concerned, in spite of the publication over the years of an impressive number of freeze–fracture electron micrographs of lipid-containing systems apparently exhibiting cubic symmetry (reviewed in [10, 11]), the *interpretation* of these in terms of the original structure is relatively recent [12, 13].

This work describes a combined freeze–fracture and X-ray scattering approach to the structural analysis of cubic phases: in particular, it deals with the phase Q^{230} (space group Ia3d), whose structure was first proposed in 1967 [14] and is now widely accepted. This structure (see figure 1) consists of a pair of three dimensional chiral labyrinths, intertwined but unconnected, related to each other by an inversion centre and separated by a septum. The two labyrinths are disjoined and are filled either by the

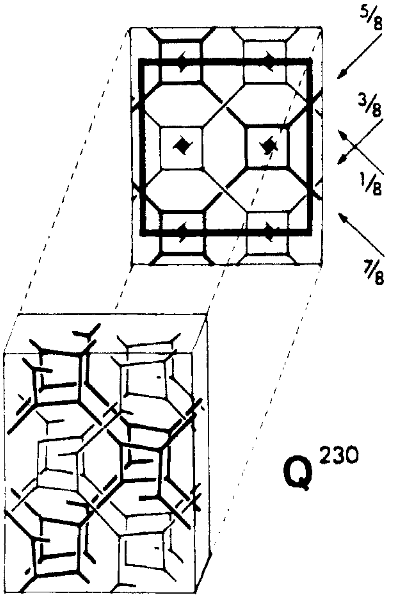

Figure 1. Schematic representation of the structure of the phase Q^{230} (Ia3d). The heavy lines mark the projection of the unit cell: some of the symmetry elements are shown. The content of the box (defined by the light lines) is shown in projection and perspective. The structure is represented in terms of two 3-D networks of rods mutually intertwined and unconnected. The rods are joined coplanarly 3 by 3. One of the networks is drawn with heavy lines, the other with light lines.

polar or by the hydrocarbon moiety: the polar headgroups of the lipid molecules lie on the interface between the labyrinths and the septum. Two chemically distinct patterns of molecular distribution are compatible with this structure: in one (the structure of type I), the interior of the labyrinths is occupied by the paraffins and the septum is filled by the polar medium; in the other (the structure of type II), the distribution is reversed. For the sake of simplicity, we will describe each labyrinth as a three dimensional network of identical rods, joined co-planarly 3 by 3. An alternative description can be given in terms of periodic minimal surfaces [15].

All cubic phases could, in principle, display distributions of type I or II, but only phase Q^{230} is known to display these two types of structure, depending on the chemical nature of the lipid. This prompted us to choose the Q^{230} phase for this work using oleoyl lysolecithin (OLPC) and egg lecithin (EggPC) whose Q^{230} phases are respectively of type I and type II.

In general, in lipid–water systems, the intrinsic resolution of freeze–fracture electron micrographs is low. In some cases, a local two dimensional periodic order is observed which in principle allows the images to be filtered and enhanced. Image processing of such arrays has been limited in the past to Fourier filtering, with rather poor results. In this work, we used a more sophisticated approach, based on correlation averaging and on a systematic comparison with the electron density maps obtained from X-ray diffraction study of the same samples.

2. Materials and methods

2.1. *Notations and abbreviations*

OLPC	Oleoyl Lyso Phosphatidyl Choline (oleoyl lysolecithin);
EggPC	Egg yolk Phosphatidyl Choline (egg lecithin);
2-D, 3-D	2 dimensional, 3 dimensional;
H, Q^n	2-D hexagonal, 3-D cubic phase of space group $N^0 n$ (International tables [16]);
type I (*and II*)	structure with the hydrocarbon chains inside the structure elements (oil in water) (*and vice versa*, (*water in oil*));
c	weight concentration (lipid/(lipid + water));
a	unit cell parameter;
$\mathbf{h}, \mathbf{s}_\mathbf{h}$	vectors which specify the reciprocal lattice point ($\mathbf{h} = \{h, k, l\}$);
$\mathbf{v}, \mathbf{w}, \gamma$	vectors and angle defining the apparent 2-D lattice on the fracture plane of the electron micrographs;
$\mathbf{t}$	vector normal to the plane of the fracture (i.e. normal to $\mathbf{v}$ and $\mathbf{w}$);
$F(\mathbf{h})$	structure factor at reciprocal lattice point $\mathbf{h}$;
β	coefficient of the gaussian apodization applied to the $\{F(\mathbf{h})\}$ that are used to compute the electron density map:

$$|F_\beta(\mathbf{h})| = [|F(\mathbf{h})| \exp(-\beta^2 \mathbf{s}_\mathbf{h}^2)]/[\Sigma_\mathbf{h} |F(\mathbf{h})|^2 \exp(-2\beta^2 \mathbf{s}_\mathbf{h}^2)]^{1/2}; \quad (1)$$

domain [*hkl*]	a selected area of the replica displaying coarse 2-D periodic order with a lattice corresponding to a planar section normal to the crystallographic direction [*hkl*]; a domain is a mosaic-like aggregate of sub-domains;
sub-domain	the strictly, periodically ordered element of a domain; a sub-domain corresponds to a single step of a fracture surface (domain).

2.2. *Preparation of the samples*

OPLC was purchased from Sigma (St. Louis, U.S.A.) and used without further purification. EggPC was prepared according to [17]. Controlled amounts of lipids and of freshly distilled water were mixed and the mixtures were kept at room temperature until equilibrium was reached. The phases were identified by X-ray scattering [6].

2.3. *Freeze–fracture electron microscopy*

Two methods were used to achieve fast cryofixation:

(1) A thin layer of the sample (less than 50 μm thick) was deposited on a thin copper holder which was then rapidly quenched in liquid propane.
(2) The sample was squeezed between two thin copper plates separated by a spacer 10 to 20 μm thick, and then rapidly quenched in liquid propane: One of the plates was scratched beforehand in order to improve the adherence. The frozen 'sandwich' was then opened under liquid nitrogen, the spacer removed and the sample adhering to the scratched plate was used for both, low temperature X-ray scattering and freeze–fracture electron microscopy (see [2] for more details).

The two types of preparation were fractured *in vacuo* (less than 7×10^{-5} Pa) with a liquid nitrogen cooled knife (maintained at 143 K), and replicated using unidirectional (at an angle of 35°) or rotary shadowing (at an angle of 25°) with tungsten–tantalum (W–Ta) alloy (about 1 nm of average metal deposit) in a Balzers 301 freeze-etching unit. The replicas were washed with organic solvents and distilled water and observed in a Philips EM 301 electron microscope. The images were recorded at a magnification of 45 000.

Most of the quantitative analysis were performed on rotary shadowed preparations, in order to avoid the anisotropic distortions introduced by unidirectional shadowing. The latter process, however, yields images with more contrast, which are highly sensitive to the structure of the sample and are therefore useful for checking the flatness of the replicas, for identifying the most frequent fracture domains and, in some cases, for revealing the relative displacement and rotation of adjacent sub-domains.

2.4. *Image selection and processing*

The freeze–fracture electron micrographs obtained had low signal to noise ratios which were improved by an image processing procedure applied to the best ordered fracture planes. All the subsequent calculations, as well as the display of the images, were performed on a VAXstation (Digital Equipment Corporation). Fourier filtering was done using the image processing program package written at the Laboratory of Molecular Biology of the MRC in Cambridge (U.K.). Real-space cross-correlation averaging and surface relief reconstruction were performed with programs locally written in Fortran and using the MRC picture format. Averaged images were visualized using SEMPER VI program package (Synoptics Ltd., Cambridge, U.K.) [18].

Freeze–fracture electron micrographs were processed by the widely used cross-correlation (CC-) averaging technique [19, 20]. The apparently best ordered areas, the domains, were selected using optical diffraction and digitized with an Optronics P1000 photoscan system at 25 μm step (pixel size 0·56 nm). Periodic areas (sub-domains) were extracted and processed according to the following procedure:

(1) The image of the sub-domain was Fourier filtered and the apparent lattice parameters **v**, **w** and γ were determined by least-square refinement from the Fourier transform.

(2) A small reference area (4 to 6 unit cells, typically 64 by 64 pixels) was extracted from the filtered image and embedded in an area of average intensity, whose size was the same as that of the image of the sub-domain.

(3) The cross-correlation map was calculated between the reference area and the sub-domain.

(4) The positions of the correlation peaks on the correlation map were determined by an automated search procedure.

(5) An averaged motif was calculated by adding image regions centred on the peak positions. No refinement step was used, since the Fourier filtering step (step (1)) had replaced the usual preliminary averaging step. An automated search procedure capable of correctly finding the correlation peaks (step (4)), even in severely distorted lattices, was designed. During the search process, the lattice parameters were used to predict the location of the next peak from the position of the peaks already located and image distortions were continuously introduced. A thorough analysis of the peak shape and of the peak to background ratio was also necessary to discriminate a true correlation peak from a false (noisy) maximum. Finally, the peak amplitudes were sorted out and those smaller than a defined threshold rejected. In order to assess the consistency of the whole procedure, an RMS statistical analysis was undertaken during averaging (step (5)). This procedure gave an estimate of the variance of the motif over the averaged images and a measure of the homogeneity of the set of averaged fragments. This selection criterion is less sophisticated than those commonly used in higher resolution electron-microscopy studies [21, 22], but we consider it to be more appropriate here, considering the poor resolution and the low signal to noise ratios of the micrographs. In the case of unidirectional shadowing, the surface profile of the replica of the fracture face was estimated from the averaged motif using a deconvolution process based upon a simple modelling of the shadowing process, which leads to a phase correction of the Fourier coefficients [23, 24]. As reported in [23, 25], 'the reconstruction obtained would be expected to resemble the surface relief, placing structural features in their correct locations, but distorting their relative elevations'. Note that in the resulting image, the lighter regions correspond to parts of lower elevation and dark regions to parts of higher elevation (this unusual convention enables a direct comparison of the surface profile motif with the rotary shadowed motif).

2.5. *Electron density maps*

The stucture of the Q^{230} phase is obtained in the form of electron density maps, computed from the observed amplitudes of the reflections and the phases determined using the pattern recognition technique described by Luzzati *et al.* [26]. For the type II structure observed in the EggPC–water system the amplitude and the sign of the reflections were taken from [6]. The crystallographic analysis of the type I Q^{230} phase observed in the OLPC–water system was carried out particularly for this study

X-ray crystallographic data. Normalized and apodized structure factors $F_{\beta}(h,k,l)$ (see equation 1), obtained from the observed intensities ([26] and Mariani *et al.*, in preparation) used to compute the 3-D electron density maps and their corresponding 2-D sections (1 Å = 0·1 nm). $C_{v,pol}$ refers to the lipid volume concentration in the sample [6].

Lipid	OLPC	Egg–PC
c	0·77	0·97
$c_{v,pol}$	0·55	0·30
T/°C	20	82
a/Å	113·1	96·2
β^2/Å^2	1842·1	277·3
type	I	II
$F(2,1,1)(10^{-3})$	+158	−186
$F(2,2,0)(10^{-3})$	+173	−108
$F(3,2,1)(10^{-3})$	−4	+11
$F(4,0,0)(10^{-3})$	−12	+21
$F(4,2,0)(10^{-3})$	−25	0
$F(3,3,2)(10^{-3})$	+27	0
$F(4,2,2)(10^{-3})$	0	0
$F(4,3,1)(10^{-3})$	+12	—
$F(5,2,1)(10^{-3})$	0	—
$F(4,4,0)(10^{-3})$	0	—

(Mariani *et al.*, in preparation). All the structural data are reported in the table. We make extensive use in this study of 2-D sections of the 3-D electron density distribution which are compared to the filtered micrographs. More precisely, we compute a normalized dimensionless expression of the fluctuations of the electron density distribution, called the electron density map (see equation 1 and also [6]). The table lists the sign and the amplitude of the structure factors (properly apodized and normalized) used in our calculations. A large number of 2-D sections of the electron density map are shown in this paper. These show equally spaced electron density levels (with an increment of 0·5 unit); the negative levels which correspond to the low-electron dense regions (roughly the paraffinic moiety) are shown as dashed lines; the zero level is represented by a full line. For the sake of clarity, the positive levels are omitted in the drawings.

3. Results

3.1. *Phase Q^{230} type I (OLPC-water, c = 0·78)*

3.1.1. *Structure preservation and the general aspect of the replicas*

The degree of preservation of the structure of this phase during the freezing process was investigated by comparing X-ray diffraction patterns of the same sample, before and after freezing. The results (reported, for example, in [12]) showed that the positions and relative intensities of the first two reflections are largely preserved, indicating that the structure remains essentially the same during freezing. The freeze–fracture replicas display complex fractures, as shown in figures 2, 5, 7 or 9. In most cases, the fracture surfaces are discontinuous and, when observed using stereo-pair images, look like the well defined cleavage planes of 3-D crystals. Clearly, caution is required in selecting suitable images for processing in order to avoid the distortions due to the plane of the fracture being tilted with respect to the plane of the replica.

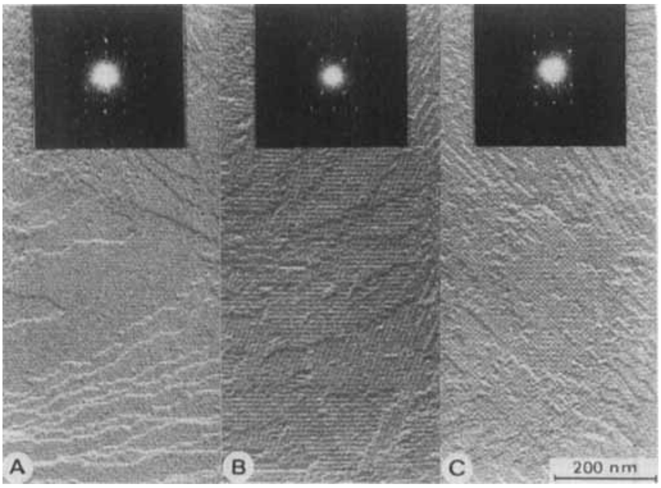

Figure 2. Freeze-fracture images of the main fracture planes (domains) observed in phase Q^{230}, type I, of the OLPC-water system ($c = 0{\cdot}78$) with unidirectional shadowing. (*A*), (*B*) and (*C*) show typical views of domains perpendicular to the crystallographic axes [211], [110] and [100], respectively. Black and white contrast corresponds to metal deposit and shadow, respectively. Inset: Corresponding optical diffractions; note the intrinsic low resolution of the images.

More or less extended, relatively flat, domains were commonly observed. According to their optical diffraction patterns and the dimensions of the 2-D unit cells, all the domains can be sorted into three classes corresponding to fracture planes normal to the crystallographic axes [211], [110] and [100] of a body-centred cubic lattice (see figure 2). Upon closer inspection, each of these domains was found to be a mosaic of sub-domains containing 2-D periodic order. Optical diffraction revealed that the 2-D lattices of all these sub-domains have the same orientation and the same dimensions. Further, within one domain, the sub-domains were found to be geometrically related to each other by simple crystallographic operations related to the lattice and to the symmetry operations. Within domains of the same class, the lattice dimensions and the symmetry elements, as well as the CC-averaged images were found to be highly reproducible.

3.1.2. *Domains [211]*

Fairly extended domains of this class were frequently observed, in which parallel striations were visible, as shown in figures 2(*A*) and 3(*A*) (unidirectional shadowing) and in figures 3(*B*) and 5(*A*) (rotary shadowing). The lattice parameters are consistent with the ideal values ($\mathbf{v} = a\sqrt{2}$, $\mathbf{w} = a\sqrt{3/2}$, $\gamma = 90°$) of the crystallographic plane [211]. The correlation map (see, for example, figure 5) shows that the fracture surfaces consist of sub-domains containing 2-D periodically ordered identical motifs, all parallel to each other and organized according to the same lattice, but slightly displaced with respect to each other.

The averaged images, obtained by processing the unidirectionally and rotary shadowed fracture planes, display identical lattices but slightly different motifs (see figures 3(*C*) and (*E*), respectively). Moreover, with unidirectional shadowing, the appearance of the motif strongly depends upon the orientation of the shadowing with

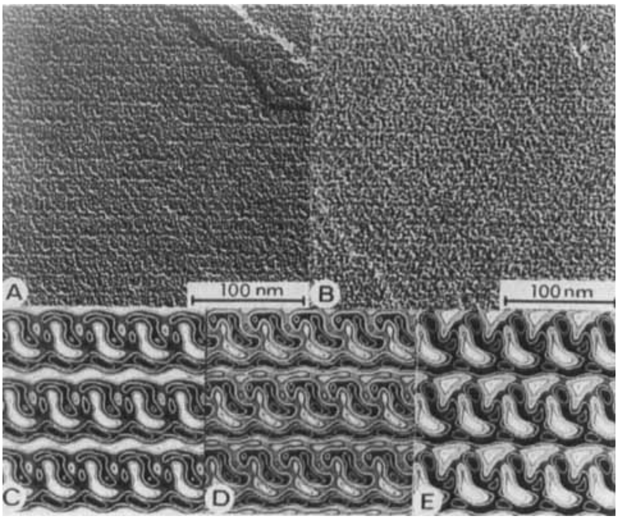

Figure 3. System and phase as in figure 2; domain [211]. Unidirectionally (*A*) and rotary (*B*) shadowed replica showing the characteristic parallel striations. (*C*) shows the correlation-averaged motif from (*A*) and (*D*), the surface relief restitution computed from (*C*) (see Materials and Methods): 'valleys' appear brighter than 'mountains'. (*E*) displays the correlation-averaged motif from frame (*B*) (note that his motif looks similar to the surface motif shown in frame (*D*)).

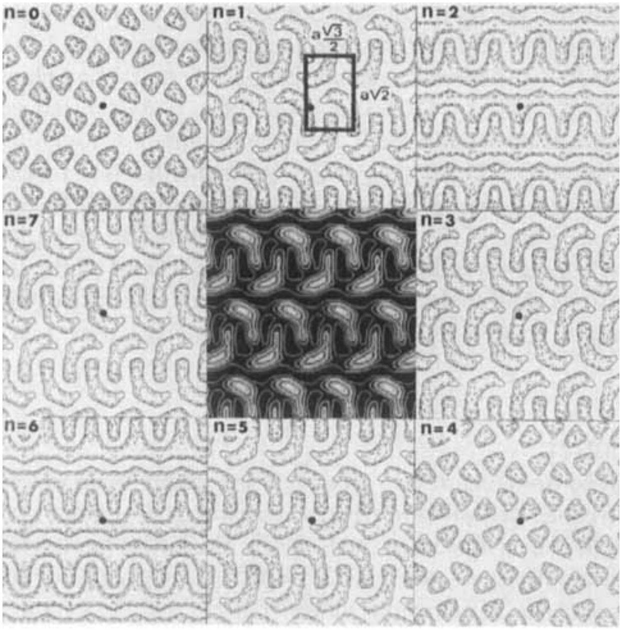

Figure 4. System and phase as in figures 2 and 3; domain [211]. Sections $n=0$ to 7. 2-D successive sections of the 3-D electron density map, in planes normal to the crystallographic axis [211] (**t**). The section ($n=0$) contains the origin (0,0,0); the position of the sections on the axis **t** is $(n/4)^*(a/\sqrt{6})$ (n is an integer). In each section, the dots mark the projection of the crystallographic origin. Note that the repeat distance along **t** is $a\sqrt{6}$ (sections drawn at positions n and $n+4$ are similar but shifted by $\mathbf{v}/3+\mathbf{w}/2$ in the plane $\{\mathbf{v},\mathbf{w}\}$). Central section: Correlation-averaged motif obtained from one of the rotary shadowed steps of the fracture surface. This motif is similar to the one observed in sections ($n=1$) and ($n=5$) of the map (note that sections ($n=3$) and ($n=7$) are mirror images of the averaged motif).

respect to the lattice. These differences could be reduced by the application of the surface restoration process (see figure 3 (*D*)).

Sections of the electron density map and the processed electron micrographs are compared in figure 4 in order to identify the nature of the structural elements appearing on this fracture plane and to determine the position of the fracture within the structure. Along the axis [211], the projection of the electron density map is a periodic function with a repeat of $a\sqrt{6}$. Some 2-D sections perpendicular to this axis are shown in figure 4. The position of any section on the **t** axis is given by $(n/4)^*(a\sqrt{6})$ (n being an integer). An excellent agreement in shape and position is observed between the bright regions of the filtered motif and the negative (paraffinic) parts of the sections ($n=1$) or ($n=5$) of the 3-D map (and also with the negative parts of the sections ($n=3$) and ($n=7$) which are the mirror images of the sections ($n=1$) and ($n=5$)). Note that the filtered images contain elongated bright regions in the positions of the paraffinic rods.

Any 2-D section of the map, normal to the direction [211] at the position t, is related to any other section at $t_n = t + n^*(a/\sqrt{6})$ (n being an integer) by a displacement $n^*(a/\sqrt{6})$ in the direction **t** and a displacement $n^*(\mathbf{v}/3 + \mathbf{w}/2)$ in the plane $\{\mathbf{v}, \mathbf{w}\}$ (as shown in figures 5 and 6). Therefore, the basic motif may have any one of six different positions with respect to the trace of **t** (projection of the origin (0, 0, 0) on the section). These shifts are in fact observed on the correlation maps (see figure 5). The height of the steps is $a/\sqrt{6}$.

3.1.3. *Domains [110]*

These domains are less extended and are composed of smaller subdomains than the domains [211]. Examples are shown in figures 2 and 8 for unidirectional and rotary shadowing, respectively. The lattice parameters are consistent with the ideal values

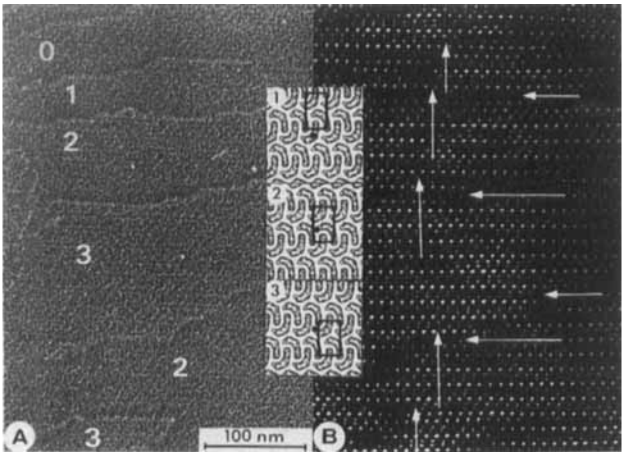

Figure 5. System and phase as in figures 2 and 4; domain [211]. (*A*); Electron micrograph of a rotary shadowed replica: note the presence of many successive steps (sub-domains labelled from 0 to 3 in the figure). Insets; successive sections of the map in planes normal to [211] (**t**) (corresponding to n, $n+4$ and $n+8$, respectively, with the conventions of figure 4): the distance along **t** between two successive sections is $a/\sqrt{6}$; the dots mark the projection of the origin on the sections. (See also figure 6). (*B*); Cross-correlation map showing the shifts between successive steps. The shifts in the directions **v** and **w** are marked by white arrows. Note how faithfully the correlation map reveals the apparent sliding of the lattices $(\mathbf{v}/3 + \mathbf{w}/2)$ between adjacent fracture steps.

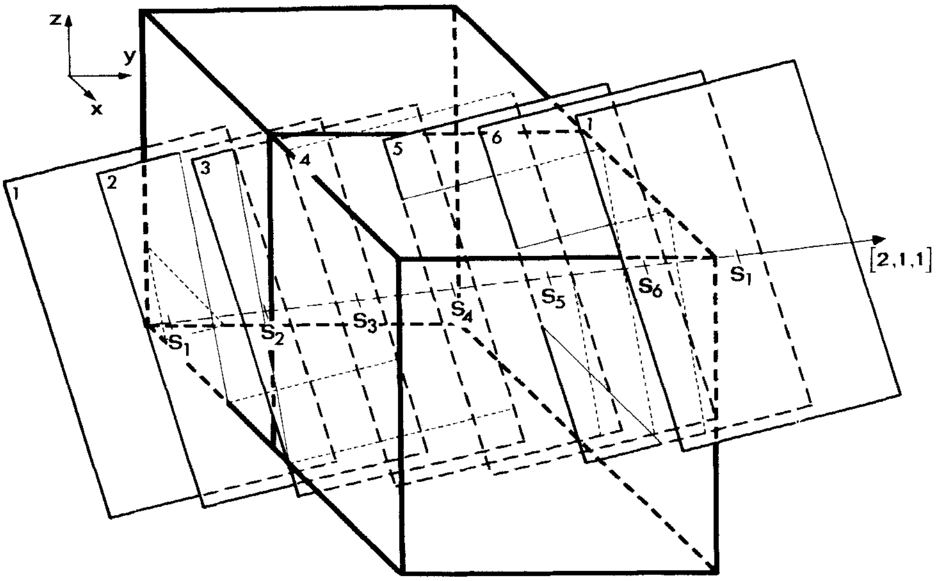

Figure 6. Schematic perspective drawing showing 2 cubic unit cells and the succession of the crystallographically equivalent sections along the axis [211]. The trace of the crystallographic axis [211] is labelled S_1, S_2, S_3, S_4, S_5 and S_6 in the successive sections.

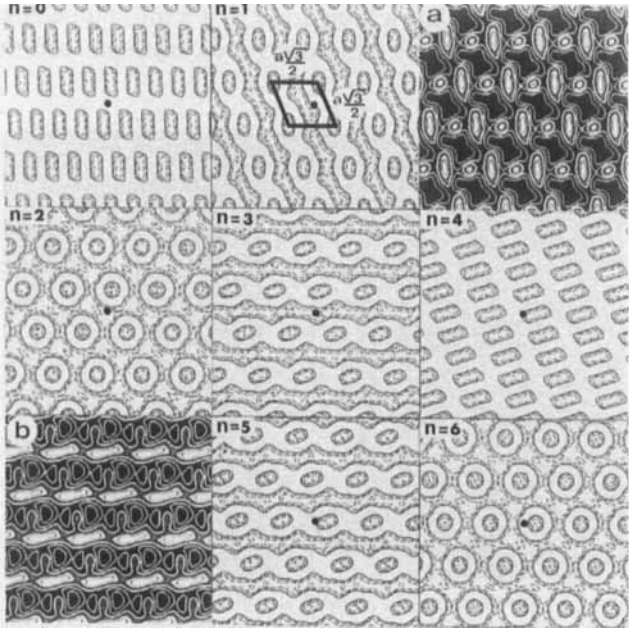

Figure 7. System and phase as in figures 2 to 5; domain [110]. Sections $n=0$ to 6: 2-D successive sections of the 3-D map normal to the crystallographic axis [110] (**t**). Section ($n=0$) contains the origin (0, 0, 0); the position of the sections on the axis **t** is $(n/4)^*(a/\sqrt{8})$ (n is an integer). The dots mark the projection of the crystallographic origin on the sections. Note that the repeat distance along **t** is $a\sqrt{2}$. Sections (*a*) and (*b*); typical aspect of the two different motifs obtained using correlation averaging on the different steps of a rotary shadowed fracture surface. Note the good agreement in position and shape of the bright regions of motif (*a*) and motif (*b*) with the negative parts of the section ($n=1$) and of the section ($n=5$) of the 3-D map, respectively. Note that the two motifs (*a*) and (*b*) are related by a mirror symmetry along the direction $\mathbf{v}+\mathbf{w}$.

($\mathbf{v}=\mathbf{w}=a\sqrt{3}/2$, $\gamma=109{\cdot}47°$) of the crystallographic plane [110]. Image processing of each sub-domain yields a motif which contains a 2-fold axis. Images of different sub-domains yield motifs which belong to two classes related to each other by a mirror line parallel to the diagonal vector $\mathbf{v}+\mathbf{w}$ (see figure 7 (*a*) and (*b*)).

The electron density map and processed images are compared in figure 7. The projection of the map on to the axis [110] is a periodic function with repeat $a/\sqrt{8}$. The 2-D sections of the map by planes normal to [110] are drawn along the $\mathbf{t}$ axis at positions $(n/4)*(a/\sqrt{8})$ (n being an integer). Good correlation is found between the shape and the position of the bright regions of the reconstructed images and those of the paraffinic (negative) parts of the section ($n=1$) for the motif (*a*) (and with the section ($n=5$) for the motif (*b*), its mirror image). In this case, the correlation averaged motif also

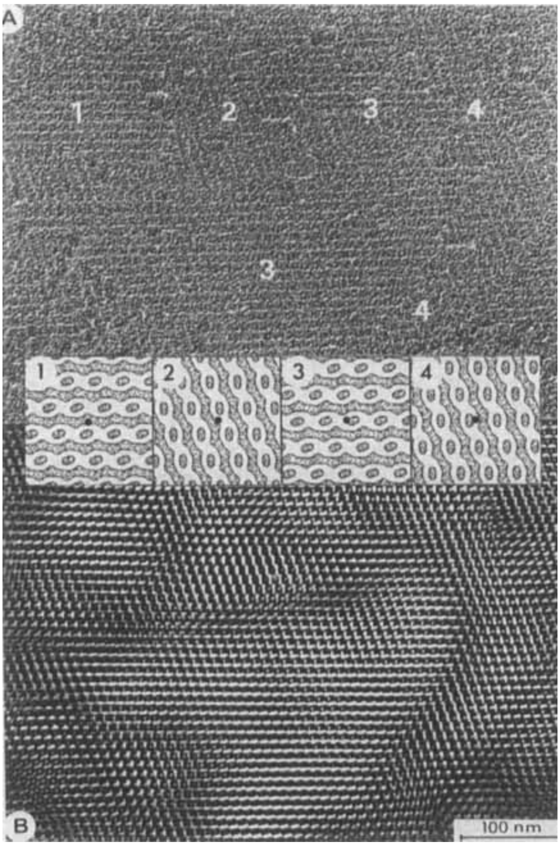

Figure 8. System and phase as in figure 7; domain [110]. (*A*); Rotary shadowed replica: note the presence of 2-D periodically ordered sub-domains (labelled from 1 to 4 in the figure) showing lozenge-like striations. Insets; section of the map in planes normal to [110] (**t**) (see figure 7); the dots mark the projection of the crystallographic origin on the sections. The distance along **t** between two successive sections is $a\sqrt{2}/4$. Note that similar lattices are shifted by $\mathbf{v}/2+\mathbf{w}/2$. (*B*); Fourier filtering of the whole of (*A*) revealing the contents of the periodic fracture steps: note, when going from left to right of the upper part of this frame, the excellent correlation of the aspect of the periodic motifs with the contents of the successive sections of the 3-D map shown in inset (regions 1 to 4 in the image correspond to the sections 1 to 4 in the insets and in figure 9).

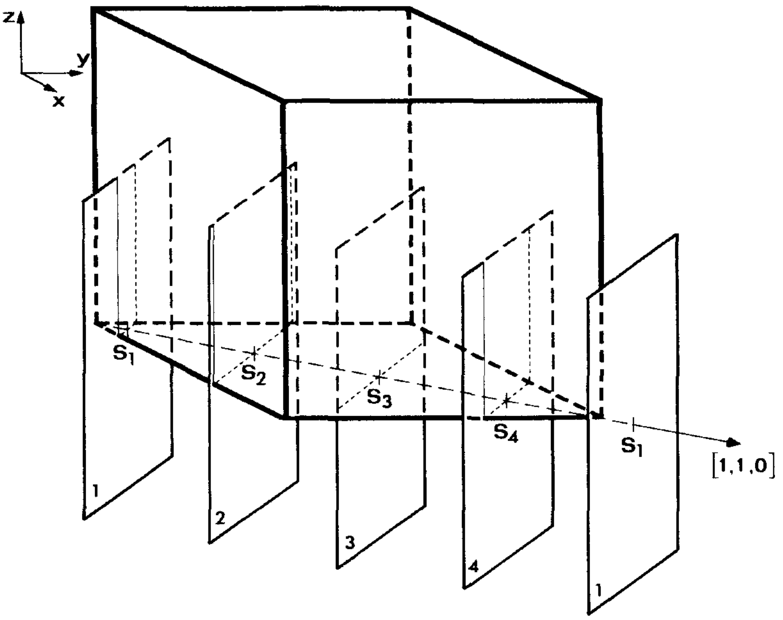

Figure 9. Schematic perspective drawing showing the cubic unit cell and the succession of the crystallographically equivalent sections along the axis [110]. The trace of the crystallographic axis [110] is labelled S_1, S_2, S_3 and S_4 in the successive sections.

displays elongated bright parts in the positions of the paraffinic rods, as well as a central bright spot at the position of a cross-sectioned rod.

The two different classes of motifs are apparent in figure 8. The Fourier filtered image (see figure 8 (*B*)) shows *that these motifs alternate in the successive areas of the fracture surface*, i.e. that the successive areas of the fracture surface contain, alternately, the two classes of motifs. The repeat along [110] is 4 times the repeat of the projection of the electron density map on [110] (see figure 9). The 2-D sections of the map by the planes normal to [110] drawn at positions $(n-1)^*(a/\sqrt{8})$ are represented in the inset of figure 8. The parameters and the orientation of the lattice are the same throughout the fracture plane. The motifs have the same orientation in each of the pairs $(n=1)/(n=3)$ and $(n=2)/(n=4)$: the two pairs, moreover, are mirror images of each other. The position of the trace of the vector **t** is shifted by **v**/2 in moving from section $(n=2)$ to $(n=3)$ and by **w**/2, in moving from sections $(n=1)$ to $(n=2)$ or $(n=3)$ to $(n=4)$. Upon close inspection of the filtered image (see figure 8 (*B*)), some of the ordered areas are found to follow the succession of motifs shown in the inset. The motifs (*a*) and (*b*) are found alternately when going from left to right, and the shifts of **v**/2 and **w**/2 in the plane $\{\mathbf{v}, \mathbf{w}\}$ are clearly visible. It may thus be concluded that the fracture consists of steps, all normal to [110], with height $a/\sqrt{8}$. Note that, in some cases, the succession of motifs between adjacent areas is broken. In these cases, the two neighbouring areas contain the same motif and the shift, which is equal to $\mathbf{v}/2+\mathbf{w}/2$, indicates that the height of the step is $2^*(a/\sqrt{8})$ and that the fracture jumped two steps.

3.1.4. *Domains [100]*

The fracture planes corresponding to these domains show fragmented, small subdomains, as is clearly visualized with unidirectional shadowing (see, for example, figures 2 and 11). The lattice parameters of these sub-domains are consistent with the ideal values ($\mathbf{v} = \mathbf{w} = a, \gamma = 90°$) of the crystallographic plane [100]. Image processing of any of the small sub-domains yields a motif which contains a 2-fold axis. Images of different sub-domains yield motifs which belong to two classes, related by a rotation of 90° (see figure 10 (*a*) and (*b*)).

The processed images and the sections of the electron density map are compared in figure 10. In this case, the projection of the map on the axis [100] is a periodic function with repeat $a/4$. The 2-D sections of the map by planes normal to [100] are drawn along the **t** axis at positions $(n/4)^*(a/4)$ (see figure 10). Good agreement is found between the shape and position of the bright regions of the averaged images obtained from rotary shadowing, and those of the paraffinic (negative) parts of the section ($n = 3$) for the motif (*a*) and of the section ($n = 7$) for the motif (*b*), its rotated image. In this case also, the filtered motifs display elongated bright regions at the positions of the paraffinic rods.

The two different classes of motifs are visualized in figure 11, where a unidirectionally shadowed fracture plane has been cross-related with a filtered fragment, corresponding to the motif (*a*). Unidirectional shadowing was preferred in this case, as it enhanced the differences between the classes of motifs. The successive fragments of the fracture surface [100] are clearly visible on the replica (see figure 11 (*A*)). The cross-correlation map (see figure 11 (*B*)) reveals two classes of periodic areas: one class where

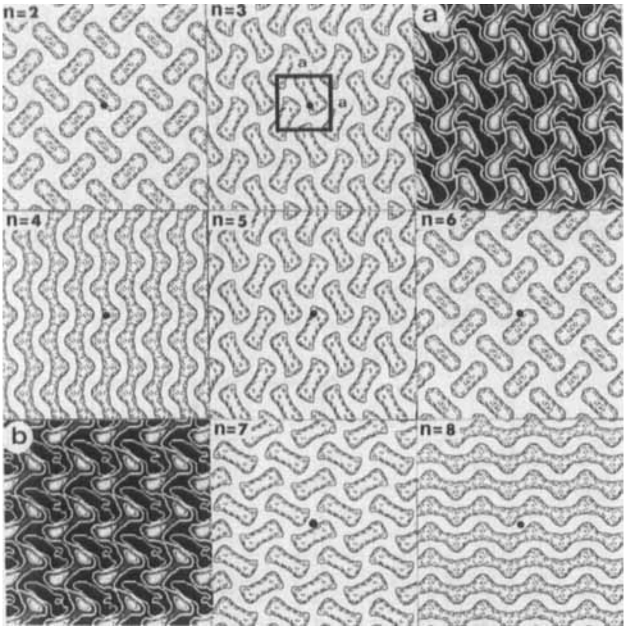

Figure 10. System and phase as in figures 7 and 8; domain [100]. Sections $n = 2$ to 8; 2-D successive sections of the 3-D electron density map planes normal to the crystallographic axis [100] (**t**). The section ($n = 2$) contains the point $(a/8, 0, 0)$; the position of the sections along **t** is $(n/4)^*(a/4)$ (n is an integer). The dots mark the projection of the crystallographic origin on the sections. Note that the repeat distance along **t** is a. Shown in (*a*) and (*b*) are typical views of the two different motifs obtained using correlation averaging on the different steps of a rotary shadowed fracture surface. Note the good agreement in position and shape of the bright regions of motif (*a*) and motif (*b*) with the negative parts of the section ($n = 3$) and of the section ($n = 7$) of the 3-D map, respectively. Note also that the two motifs (*a*) and (*b*) are related by a rotation of 90° around $(0, a/4)$.

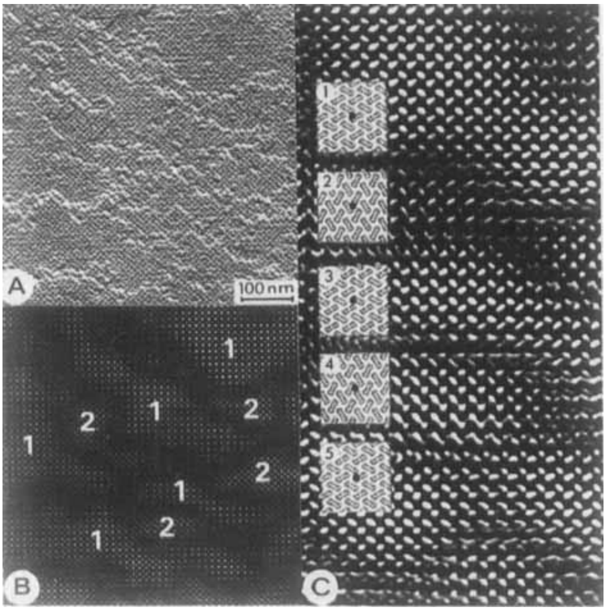

Figure 11. System and phase as in figure 10; domain [100]. (*A*); Unidirectionally shadowed replica. (*B*); Cross correlation map from image (*A*) note the presence of 2-D periodically ordered patches (labelled 1 and 2 for motif (*a*) and (*b*), respectively). Insets; sections of the 3-D map normal to the axis [100] (see figures 10 and 12) drawn at the scale of (*C*): the dots mark the projection of the crystallographic origin on the sections; the size of each section is 4*a**4*a*; the distance between the successive sections along **w** is a; the distance along **t** between two successive sections is *a*/4. (*C*); Fourier filtered and enlarged image of the central part of (*A*). The presence of the two different aspects of the periodic motifs is emphasized. Note the excellent correlation in shape and position between the bright regions of the filtered periodic motifs and the negative parts of the successive sections of the 3-D map drawn in inset (at the same scale and in register with the fracture steps).

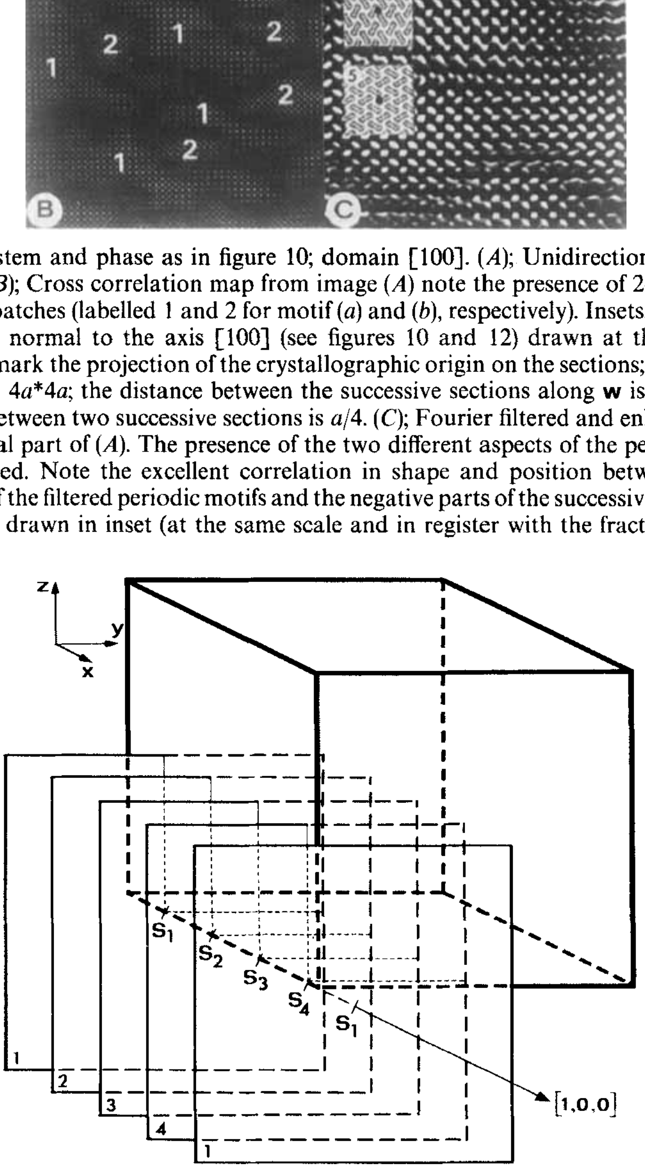

Figure 12. Schematic perspective drawing showing the cubic unit cell and the succession of the crystallographically equivalent sections along the axis [100]. The trace of the crystallographic axis [100] is labelled S_1, S_2, S_3 and S_4 in the successive sections.

the correlations are clear, corresponds to areas which contain the motif (*a*), and another class where the correlations are weaker, corresponds to areas which contain the slightly different motif (*b*). The alternation of motifs (*a*) and (*b*) is clearly visible in the Fourier filtered and enlarged image shown in figure 11 (*C*), which also shows that the relative shift in the plane $\{\mathbf{v}, \mathbf{w}\}$ between successive areas containing the same motif is half of a unit cell ($\mathbf{v}/2+\mathbf{w}/2$). The corresponding (successive) and equivalent sections of the electron density map (see figure 12) are shown on the same scale, in the inset, to demonstrate the fidelity with which the fracture reveals the local structure of the cubic phase and the presence of a 4-fold screw axis (situated at $(0, a/4)$ in the cubic lattice). The height of the step is $a/4$. However, it can be often observed that the fracture climbs two steps at a time as contiguous fracture steps were found to contain the same motif, but with an apparent translation ($\mathbf{v}/2+\mathbf{w}/2$).

3.2. *Phase Q^{230} type II (Egg PC–water, $c=0{\cdot}95$)*

The phase diagram of the EggPC–water system displays, at low water content, a cubic phase Q^{230}, which is known to be of type II [27]. The preservation of this phase through cryofixation has been shown to be excellent [3].

The freeze–fracture images display large and flat areas with parallel striations (see figures 13 and 14) or patchworks of small periodic surfaces containing a lozenge-like motif (see figure 15). A closer inspection reveals that these different views correspond to two different fracture planes, respectively perpendicular to the crystallographic directions [211] and [110]. As already mentioned for the type I structure, the fracture plane [211] is also the most frequently observed here.

3.2.1. *Domains [211]*

Figure 13 shows two micrographs of the domains [211] obtained using unidirectionally (*A*) and rotary (*B*) shadowing of the fracture, along with the corresponding filtered images: corresponding correlation averaged motifs are shown in (*C*) and (*E*), respectively. A tentative restoration of the surface profile corresponding to (*C*) is shown in (*D*). The aspects of these motifs differ from the corresponding motifs of the type I structure (see figures 4 (*C*), (*D*) and (*E*)). The contrast in one set of motifs is inverted with respect to that of the other set of motifs. 2-D sections of the electron density map drawn perpendicularly to the axis [211] ($\mathbf{t}$) at successive positions $(n/8)^*(a/\sqrt{6})$ are shown in the bottom of figure 13. Good agreement is found among the shapes and the positions of the dark regions of the filtered motifs and those of the positive parts of the sections which are close to the origin (0, 0, 0). Note that, as in the type I structure, bright regions of the averaged motifs correspond to the paraffinic parts in the 2-D sections of the 3-D map. These results differ from the ones obtained for the type I structure, suggesting that the fracture propagates via different pathways in this crystallographic direction in the type I and type II structures. However, the same succession of regular apparent translations between adjacent fracture steps, is revealed on the correlation map shown in figure 14.

3.2.2. *Domains [110]*

These domains display small periodically ordered areas, as shown in figure 15. The optical diffraction pattern (see the inset in figure 15) indicates the presence of rather poorly ordered sub-domains displaying 2-D lattice parameters corresponding to the crystallographic plane [100]. The fragmented and distorted nature of these fracture surfaces precludes any attempt to get faithful information about the local aspect of

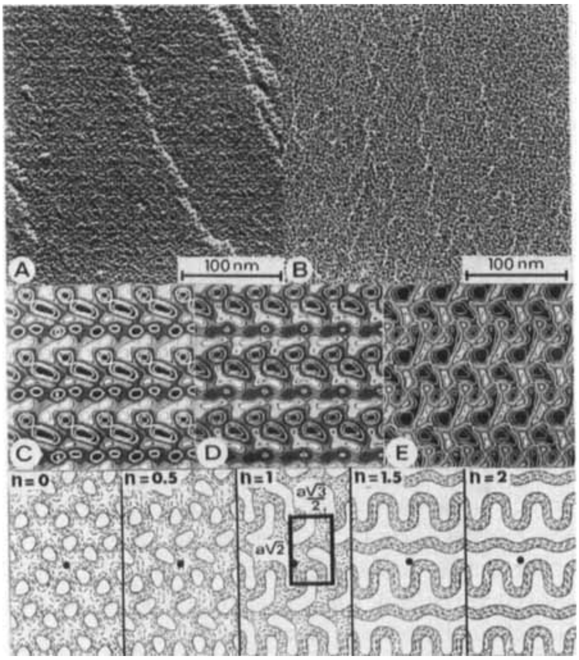

Figure 13. Unidirectionally (*A*) and rotary (*B*) shadowed fragments of fracture planes perpendicular to the crystallographic axis [211] of the Q^{230} type II EggPC–water ($c=0{\cdot}95$) phase. (*C*) shows the correlation-averaged motif from image (*A*); (*D*), the surface relief restitution from (*C*); and (*E*), the correlation averaged motif from image (*B*): note that its aspect is quite similar to the surface motif shown in (*D*). Sections $n=0$ to 2: successive 2-D section of the 3-D electron density map normal to crystallographic axis [211] (**t**). The section ($n=0$) contains the origin (0, 0, 0); the position of the sections on the axis **t** is $(n/8)^*(a/\sqrt{6})$ ($n=0, 0{\cdot}5, 1, 1{\cdot}5$ and 2). The dots mark the projection of the crystallographic origin of the sections. Note the good agreement in position and shape, of the dark regions of the filtered motifs with the positive parts of the sections ($n=0$) and ($n=0{\cdot}5$) which are close to the origin of the 3-D map.

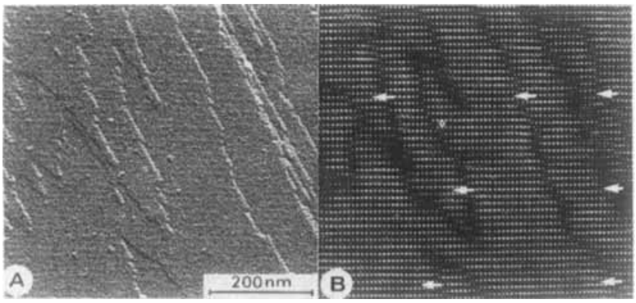

Figure 14. System and phase as in figure 13; domain [211]. Shown in (*A*) is a unidirectionally shadowed replica containing a succession of fracture steps. (*B*) is a cross-correlation map from image (*A*). Note that the different fracture steps are, as in type I, related to each other by apparent slidings between the periodic motifs; white arrows indicate the shifts between contiguous fracture surface steps in the direction **w**.

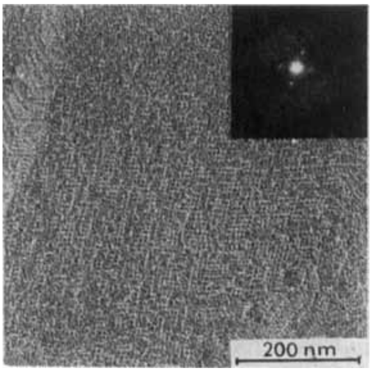

Figure 15. System and phase as in figures 13 and 14; domain [110]. Unidirectionally shadowed replica. Inset: corresponding optical diffraction pattern.

these domains using image filtering and may explain why we did not succeed in observing it on rotary shadowed replicas which are more appropriate for the image analysis.

4. Discussion

Although freeze–fracture electron microscopy is commonly used in the study of lipid–water phases, the images are rarely processed and analysed as in other areas of electron microscopy. The starting hypothesis of our work [12] is that the information content of the micrographs is worth the effort of processing. The results obtained on both type I and type II Q^{230} phases, give an *a posteriori* justification of our conviction.

For the sake of clarity, we discuss the results concerning the different aspects of this work separately. As most of the results concern the type I structure, the discussion is focused on this structure. At the end, the differences concerning the type II structure are pointed out.

4.1. *Phase* Q^{230} *type I (OLPC–water,* $c = 0{\cdot}78$*)*

4.1.1. *Structure preservation*

Structures of type I generally contain a large amount of water and their preservation during the freeze–fracture process may be a serious problem [2, 3]. The results obtained with OLPC containing 22 per cent water, indicate that the 3-D cubic structure may be well preserved not only after cryofixation, as assessed by low temperature X-ray experiments [12], but also after the fracturing and the replicating processes. Freeze–fracture replicas reveal, indeed, the presence of planar domains, periodically ordered, which, according to the (optical) diffraction patterns and to the dimensions of the 2-D unit cells, correspond to a few preferential crystallographic orientations of the cubic lattice. The cell parameters computed from a large number of micrographs ($a = 11{\cdot}14 \pm 0{\cdot}10$ nm for OLPC) confirm the reproducibility of the experiments and indicate that the whole process induces only a slight shrinking of the samples (less than 2 per cent). Furthermore, the preservation of the cubic structure is corroborated by the fact that the freeze–fracture micrographs allow the direct observation of most of the symmetries of the cubic space group, as well as the correlation between the content of the fracture domains and the structure elements of the cubic phase as discussed below.

4.1.2. *Symmetry*

As already noted [12] in the case of the domains [211], the symmetry properties of the EM images mirror the symmetry of the space group. One of the most interesting symmetry elements revealed by this analysis is the 4-fold screw axis along the axis [100] which is one of the most characteristic symmetries of the Ia3d space group. In the CC-averaged motifs, we have also established the presence of a 2-fold axis in the directions [100] and [110]. The analysis of the different domains by cross-correlation or Fourier filtering techniques has shown shifts, mirrors and rotations between adjacent sub-domains that are clearly related to the symmetries of the group. Note that the information regarding symmetry is, to a large extent, independent of the correlations between the EM images and the structure of the sample, which are discussed below.

4.1.3. *Comparison and correlations between the processed images and the electron density distribution*

At the very beginning of this work, the search for correlations between the CC-averaged freeze–fracture images and the planar sections of the 3-D electron density map seemed far-fetched. However, the preliminary results that we obtained on this cubic structure [12] demonstrated that the fracture surfaces mirror enough of the structure to be comparable to true sections of the structure.

Indeed, the shadowing techniques used in this work are aimed at revealing the surface features of the fractures, which are not, *a priori*, related to the electron density distribution in the corresponding planar sections of the electron density map. The justification was provided by the spectacular resemblance of the electron microscope images and the related sections of the electron density map (see figures 4, 7, 10 and 13). The reason for this resemblance is probably related to the nature of the elements (paraffinic rods) present in the structure and to the mechanism involved in the fracturing of the sample.

In the case of the structure of the OLPC–water system, three different fracture directions, corresponding to planes normal to the crystallographic axes [211], [110] and [100], were observed. For each fracture direction, image processing of either unidirectionally or rotary shadowed replicas have yielded motifs that were easily related to one section of the electron density map. In the case of rotary shadowed images, bright regions of the averaged motifs were identified as corresponding to the paraffinic parts of the structure. It is remarkable that the size and shape of the bright parts faithfully mirror those of the paraffinic parts of the corresponding sections of the electron density map. Furthermore, the surface relief reconstruction done in each case from unidirectionally shadowed replicas yielded motifs that are similar to those obtained directly from rotary shadowing and thus confirmed that the bright regions of the micrographs in rotary shadowing correspond to the region of lower elevation in the fracture surface. Therefore, those bright parts should correspond to the imprints of the paraffinic rods. Moreover, in the domains [211], those rods appear strongly connected, confirming the cage-like aspect of this cubic structure.

4.1.4. *Preferential crystallographic orientations of the domains identified in the electron micrographs*

Only three classes of well-defined fracture planes (domains) clearly displaying 2-D order were identified on the micrographs. These classes correspond to the different preferential crystallographic orientations of the fracture within the structure.

They were shown to display two main characteristics:

(1) They all belong to the family of planes [nnm] (with n and m being integers): those planes are remarkable in the sense that they all contain rods (see figure 1).
(2) They are related to the first X-ray reflections ($2n^2+m^2$ is small, see the table) and with the exception of the direction [100] which is rare, the corresponding reflections are strong, reflecting a 'stratified' structure of the elements in those directions.

4.1.5. *The mechanism involved in the fracturing, shadowing and replicating steps*

The molecular phenomena involved in the fracture of frozen lipid–water samples are relatively well understood in the case of phases ordered in one or two dimensions [3, 28, 29], but much less in the case of 3-D structures, such as the cubic phases. The problem is to discover the correlation if any, between the preferential fracture planes and the structure of the phase.

Images relevant to well-preserved fracture surfaces of type I have revealed the imprints of elongated structure elements that, for the sake of simplicity, we shall call the ' paraffinic rods' of the structure (see figure 1). The comparison between the selected electron density sections and the processed micrographs indicates that the morphology of the rods is preserved (see figures 4, 7 and 10). Therefore, the fracture may not be able to cross the rods easily, but propagates preferentially along planar layers of the structure which present a maximal content of rods, i.e. in the directions [211], [110] and [100]. Image analysis also revealed that in the structure of type I, two different sections usually related by a mirror plane, are compatible with the view of the motif (for example, sections ($n=1$) and ($n=3$) in figure 4); one corresponds to the imprint, the other to the surface relief of the rods. However, correlation techniques indicate that of the two, only the former can be observed in the best ordered fracture planes.

On the basis of these observations, it can be argued that the fractures occur along the symmetry planes containing the rods and that the networks of these rods constitute the support for propagation of the fracture. The rod networks may behave like fishbones when one tries to separate the two sides of a fish: a given fracture plane will contain only one of the two sides and the best preserved (containing imprints) will be preferentially observed (see also [12]). Recent results obtained in the case of the Q^{223} type I (Pm3n) cubic phase [13] corroborate this hypothesis.

4.2. *Phase* Q^{230} *type II (EggPC–water,* $c=0{\cdot}95$*)*

The processing of the micrographs confirmed the good preservation of this cubic structure at the end of the fracturing and replicating process.

The cell parameters computed from the micrographs ($a=9{\cdot}08\pm0{\cdot}20$ nm) show that the whole process induces only a slight shrinking of the samples (less than 5 per cent).

A close inspection of the best ordered domains revealed that only the fracture planes perpendicular to the axes [211] and [110] could be clearly identified. In this case, the resolution of the micrographs is lower but the symmetries observed in the averaged motifs and inside the domains corresponding to the orientation [211] are the same as in the type I structure. The processed images show motifs which differ from the corresponding motifs of the type I structure: the two sets of motifs look like the negatives of each other. Bright regions of these averaged motifs correspond to the paraffinic parts of the 2-D sections of the 3-D electron density map. The best correlation is found, in this case, between the shape and the position of the dark regions of the filtered motifs and those of the positive parts of the sections close to the origin. These results indicate that fracture paths for the type I and type II phases are different. However, as in the type I structure, fractures occur along the planes [*nnm*] where the *F*[*nnm*] are strong. In the EggPC–water system, these directions are [211] and [110] (see the table). The correspondence between the structural features and the bright parts of the averaged motif is not clear, as one is looking at a complex surface rather than at a set of well separated structural elements. The analysis of the fracture surfaces indicates that in the two orientations, the fracture seems to propagate along the symmetry planes of the paraffinic interface. Considering the disordered arrangement of the hydrocarbon chains, this fracture behaviour, already observed in the lamellar and in the hexagonal phases of type II, could explain the low quality of the filtered motifs of fracture planes [211] and [110].

5. Conclusion

The main conclusion which can be drawn from this work is that it is possible to preserve the crystalline order of the cubic phases during the entire freeze–fracture process and, when such preservation is achieved, the image analysis of micrographs provides an excellent approach, complementary to that of X-ray diffraction, for investigating the structure of even the most complex ordered phases containing lipids.

The authors gratefully acknowledge V. Luzzati's constant encouragement and useful discussions, as well as the excellent technical assistance from J. C. Dedieu.

References

[1] Costello, M. J., and Gulik-Krzywicki, T., 1976, *Biochim. biophys. Acta*, **455**, 412.

[2] Gulik-Krzywicki, T., and Costello, M. J., 1978, *J. Microsc.*, **112**, 103.

[3] Gulik-Krzywicki, T., Aggerbeck, L. P., and Larsson, K., 1984, *Surfactants in Solution*, Vol. 1, edited by K. L. Mittal and B. Lindman (Plenum Publishing Corporation), p. 237.

[4] Ranck, J. L., Mateu, L., Sadler, D. M., Tardieu, A., Gulik-Krzywicki, T., and Luzzati, V., 1974, *J. molec. Biol.*, **85**, 249.

[5] Verkleij, A. J., Ververgaert, P. H. J., van Deenen, L. L. M., and Elbers, P. F., 1972, *Biochim. biophys. Acta*, **288**, 326.

[6] Mariani, P., Luzzati, V., and Delacroix, H., 1988, *J. molec. Biol.*, **204**, 165.

[7] Charvolin, J., and Rigny, G., 1973, *J. chem. Phys.*, **58**, 3999.

[8] Lindblom, G., Larsson, K., Johansson, L., Fontell, K., and Forsen, S., 1979, *J. Am. chem. Soc.*, **101**, 4565.

[9] Cribier, S., Bourdieu, L., Vargas, R., Gulik, A., and Luzzati, V., 1990, *J. Phys.* C, **51**, 7105.

[10] Verkleij, A. J., 1984, *Biochim. biophys. Acta*, **779**, 43.

[11] Lindblom, G., and Rilfors, L., 1989, *Biochim. biophys. Acta*, **988**, 221.

[12] Delacroix, H., Mariani, P., and Gulik-Krzywicki, T., 1990, *J. Phys.* C, **51**, 7119.

[13] Delacroix, H., Gulik-Krzywicki, T., Mariani, P., and Luzzati, V., 1993, *J. molec. Biol.*, **229**, 526.

[14] Luzzati, V., and Spegt, P. A., 1967, *Nature, Lond.*, **215**, 701.

[15] Sadoc, J. F., and Charvolin, J., 1989, *Acta crystallogr.*, **45**, 10.

[16] *International Tables for X-ray Crystallography*, 1952 (Kynoch Press).

[17] Singleton, W. S., Gray, M. S., Brown, M. L., and White, J. L., 1965, *J. Am. Oil chem. Soc.*, **42**, 53.

[18] Saxton, W. O., Pitt, T. J., and Horner, M., 1979, *Ultramicroscopy*, **4**, 343.

[19] Saxton, W. O., and Frank, J., 1977, *Ultramicroscopy*, **2**, 219.

[20] Frank, J., Goldfarb, W., Eisenberg, D., and Baker, T. S., 1978, *Ultramicroscopy*, **3**, 283.

[21] Henderson, R., Baldwin, J. M., Downing, K. H., Lepault, J., and Zemlin, F., 1986, *Ultramicroscopy*, **19**, 147.

[22] Frank, J., Chiu, W., and Degn, L., 1988, *Ultramicroscopy*, **26**, 345.

[23] Smith, P. R., and Kistler, J., 1977, *J. Ultrastruct. Res.*, **61,** 124.

[24] Winkler, H., and Gross, H., 1988, *Image and Signal Processing in Electron Microscopy, Scanning Microscopy Supplement*, Vol. 2, (Scanning Microscopy International), p. 379.

[25] Baumeister, W., Guckenberger, R., Engelhardt, H., and Woodcock, C. L. F., 1986, *Ann. N.Y. Acad. Sci.*, **483,** 57.

[26] Luzzati, V., Mariani, P., and Delacroix, H., 1988, *Makromolek. Chem., Macromolek. Symp.*, **15,** 1.

[27] Luzzati, V., Tardieu, A., Gulik-Krzywicki, T., Rivas, E., and Reiss-Husson, F., 1968, *Nature, Lond.*, **220,** 485.

[28] Deamer, W., Leonard, R., Tardieu, A., and Branton, D., 1970, *Biochim. biophys. Acta*, **219,** 47.

[29] Gulik-Krzywicki, T., 1975, *Biochim. biophys. Acta*, **415,** 1.